The IEE

IEE Radar, Sonar and Navigation series 19

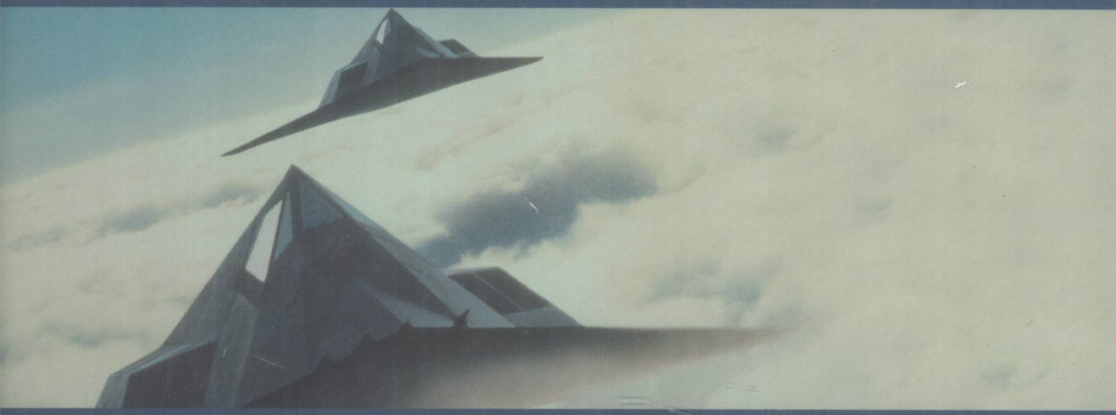

Radar Imaging and Holography

A Pasmurov and J Zinoviev

Radar Imaging and Holography

Alexander Ya. Pasmurov and
Julius S. Zinoviev

The Institution of Electrical Engineers

Published by:

The Institution of Electrical Engineers,
Michael Faraday House,
Six Hills Way, Stevenage,
Herts. SG1 2AY, United Kingdom

British Library Cataloguing in Publication Data

Pasmurov, Alexander Ya.
Radar imaging and holography
1. Radar 2. Imaging systems 3. Radar targets 4. Holography
I. Title II. Zinoviev, Julius S. III. Institution of Electrical Engineers
621.3'848

ISBN-10: 0 86341 502 4
ISBN-13: 978-086341-502-9

Typeset in India by Newgen Imaging Systems (P) Ltd., Chennai, India
Printed in the UK by MPG Books Limited, Bodmin, Cornwall

IEE RADAR, SONAR AND NAVIGATION SERIES 19

Series Editors: Dr N. Stewart
Professor H. Griffiths

Radar Imaging and Holography

Other volumes in this series:

Volume 1	**Optimised radar processors** A. Farina (Editor)
Volume 2	**Radar development to 1945** R. W. Burns (Editor)
Volume 3	**Weibull radar clutter** M. Sekine and Y. H. Mao
Volume 4	**Advanced radar techniques and systems** G. Galati (Editor)
Volume 7	**Ultrawideband radar measurements** L. Yu. Astanin and A. A. Kostylev
Volume 8	**Aviation weather surveillance systems: advanced radar and surface sensors for flight safety and air traffic management** P. Mahapatra
Volume 10	**Radar techniques using array antennas** W. D. Wirth
Volume 11	**Air and spaceborne radar systems** P. Lacomme, J. C. Marchais, J. P. Hardange and E. Normant
Volume 12	**Principles of space-time adaptive processing** R. Klemm
Volume 13	**Introduction to RF Stealth** D. Lynch
Volume 14	**Applications of space-time adaptive processing** R. Klemm (Editor)
Volume 15	**Ground penetrating radar, 2nd edition** D. J. Daniels (Editor)
Volume 16	**Target detection by marine radar** J. Briggs
Volume 17	**Strapdown inertial navigation technology** D. H. Titterton and J. L. Weston

List of tables

Chapter 6

Table 6.1 The number of spectral components of a PH 136

Chapter 8

Table 8.1 The main characteristics of the synthetic aperture pattern 174

Chapter 9

Table 9.1 Technical parameters of SARs borne by the SEASAT and Shuttle 192

Table 9.2 Parameters of the Almaz-1 SAR 192

Table 9.3 The parameters of the ERS-1/2 satellites 193

Table 9.4 SAR imaging modes of the RADARSAT satellite 194

Table 9.5 The ENVISAT ASAR operation modes 194

Table 9.6 The LRIR characteristics 216

Table 9.7 The variants of the sign vectors 227

Table 9.8 The valid recognition probability (a Bayes classifier) 228

Table 9.9 The valid recognition probability (a classifier based on the method of potential functions) 228

Contents

List of figures ix

List of tables xvii

Introduction 1

1 Basic concepts of radar imaging 7
1.1 Optical definitions 7
1.2 Holographic concepts 10
1.3 The principles of computerised tomography 14
1.4 The principles of microwave imaging 20

2 Methods of radar imaging 27
2.1 Target models 27
2.2 Basic principles of aperture synthesis 31
2.3 Methods of signal processing in imaging radar 33
2.3.1 SAR signal processing and holographic radar for earth surveys 33
2.3.2 ISAR signal processing 34
2.4 Coherent radar holographic and tomographic processing 36
2.4.1 The holographic approach 36
2.4.2 Tomographic processing in 2D viewing geometry 41

3 Quasi-holographic and holographic radar imaging of point targets on the earth surface 49
3.1 Side-looking SAR as a quasi-holographic radar 49
3.1.1 The principles of hologram recording 50
3.1.2 Image reconstruction from a microwave hologram 53
3.1.3 Effects of carrier track instabilities and object's motion on image quality 57

3.2 Front-looking holographic radar 60
3.2.1 The principles of hologram recording 60
3.2.2 Image reconstruction and scaling relations 62
3.2.3 The focal depth 67
3.3 A tomographic approach to spotlight SAR 70
3.3.1 Tomographic registration of the earth area projection 70
3.3.2 Tomographic algorithms for image reconstruction 72

4 Imaging radars and partially coherent targets 79
4.1 Imaging of extended targets 80
4.2 Mapping of rough sea surface 82
4.3 A mathematical model of imaging of partially coherent extended targets 85
4.4 Statistical characteristics of partially coherent target images 87
4.4.1 Statistical image characteristics for zero incoherent signal integration 88
4.4.2 Statistical image characteristics for incoherent signal integration 90
4.5 Viewing of low contrast partially coherent targets 94

5 Radar systems for rotating target imaging (a holographic approach) 101
5.1 Inverse synthesis of 1D microwave Fourier holograms 101
5.2 Complex 1D microwave Fourier holograms 110
5.3 Simulation of microwave Fourier holograms 112

6 Radar systems for rotating target imaging (a tomographic approach) 117
6.1 Processing in frequency and space domains 117
6.2 Processing in 3D viewing geometry: 2D and 3D imaging 119
6.2.1 The conditions for hologram recording 120
6.2.2 Preprocessing of radar data 124
6.3 Hologram processing by coherent summation of partial components 126
6.4 Processing algorithms for holograms of complex geometry 130
6.4.1 2D viewing geometry 131
6.4.2 3D viewing geometry 141

7 Imaging of targets moving in a straight line 147
7.1 The effect of partial signal coherence on the cross range resolution 148
7.2 Modelling of path instabilities of an aerodynamic target 151
7.3 Modelling of radar imaging for partially coherent signals 152

8 Phase errors and improvement of image quality **157**
8.1 Phase errors due to tropospheric and ionospheric turbulence 157
8.1.1 The refractive index distribution in the troposphere 157
8.1.2 The distribution of electron density fluctuations in the ionosphere 166
8.2 A model of phase errors in a turbulent troposphere 167
8.3 A model of phase errors in a turbulent ionosphere 172
8.4 Evaluation of image quality 173
8.4.1 Potential SAR characteristics 173
8.4.2 Radar characteristics determined from images 175
8.4.3 Integral evaluation of image quality 177
8.5 Speckle noise and its suppression 181
8.5.1 Structure and statistical characteristics of speckle 182
8.5.2 Speckle suppression 184

9 Radar imaging application **191**
9.1 The earth remote sensing 191
9.1.1 Satellite SARs 191
9.1.2 SAR sea ice monitoring in the Arctic 195
9.1.3 SAR imaging of mesoscale ocean phenomena 204
9.2 The application of inverse aperture synthesis for radar imaging 215
9.3 Measurement of target characteristics 217
9.4 Target recognition 222

References **231**

List of abbreviations **241**

Index **243**

List of figures

Chapter 1

Figure 1.1 The process of imaging by a thin lens 8

Figure 1.2 A schematic illustration of the focal depth of an optical image: (a) image of point M lying in the optical axis; (b) image of point A; (c) image of point B and (d) image of points A and B in the planes M_1, M_2 and M_3 9

Figure 1.3 The process of optical hologram recording: 1 – reference wave; 2 – object; 3 – photoplate and 4 – object's wave 11

Figure 1.4 Image reconstruction from a hologram: 1 – virtual image; 2 – real image; 3 – zero diffraction order and 4 – hologram 13

Figure 1.5 Viewing geometry in computerised tomography (from Reference 15): Γ_m – circumference for measurements; Γ_c – circumference with the centre at point O enveloping a cross section; p – arbitrary point in the circle with the polar coordinates ρ and Φ; A, C and D – wide beam transmitters; B, C′ and D′ – receivers; γ–γ, δ–δ – parallel elliptic arcs defining the resolving power of transmitter–receiver pair (CC′ and DD′) 15

Figure 1.6 A scheme of X-ray tomographic experiment using a collimated beam: 1 – X-rays; 2 – projection angle; 3 – registration line; 4 – projection axis and 5 – integration line 17

Figure 1.7 The geometrical arrangement of the $G(x,y)$ pixels in the Fourier region of a polar grid. The parameters ϑ_{max} and ϑ_{min} are the variation range of the projection angles. The shaded region is the SAR recording area 18

Figure 1.8 Synthesis of a radar aperture pattern: (a) real antenna array and (b) synthesised antenna array 22

Chapter 2

Figure 2.1 Viewing geometry for a rotating cylinder: 1, 2, 3 – scattering centres (scatterers) 30

Figure 2.2 Schematic illustrations of aperture synthesis techniques: (a) direct synthesis implemented in SAR, (b) inverse synthesis for a target moving in a straight line and (c) inverse synthesis for a rotating target 32

Figure 2.3 The holographic approach to signal recording and processing in SAR: 1 – recording of a 1D Fraunhofer or Fresnel diffraction pattern of target field in the form of a transparency (azimuthal recording of a 1D microwave hologram), 2 – 1D Fourier or Fresnel transformation, 3 – display 34

Figure 2.4 Synthesis of a microwave hologram: (a) quadratic hologram recorded at a high frequency, (b) quadratic hologram recorded at an intermediate frequency, (c) multiplicative hologram recorded at a high frequency, (d) multiplicative hologram recorded at an intermediate frequency, (e) quadrature holograms, (f) phase-only hologram 37

Figure 2.5 A block diagram of a microwave holographic receiver: 1 – reference field, 2 – reference signal $\cos(\omega_0 t + \varphi_0)$, 3 – input signal $A\cos(\omega_0 t + \varphi_0 - \varphi)$, 4 – signal $\sin(\omega_0 t + \varphi_0)$ and 5 – mixer 39

Figure 2.6 Illustration for the calculation of the phase variation of a reference wave 39

Figure 2.7 The coordinates used in target viewing 42

Figure 2.8 2D data acquisition design in the tomographic approach 45

Figure 2.9 The space frequency spectrum recorded by a coherent (microwave holographic) system. The projection slices are shifted by the value f_{po} from the coordinate origin 46

Figure 2.10 The space frequency spectrum recorded by an incoherent (tomographic) system 47

Chapter 3

Figure 3.1 A scheme illustrating the focusing properties of a Fresnel zone plate: 1 – collimated coherent light, 2 – Fresnel zone plate, 3 – virtual image, 4 – real image and 5 – zeroth-order diffraction 50

Figure 3.2 The basic geometrical relations in SAR 51

Figure 3.3 An equivalent scheme of 1D microwave hologram recording by SAR 51

Figure 3.4 The viewing field of a holographic radar 60

Figure 3.5 A schematic diagram of a front-looking holographic radar 61

Figure 3.6 The resolution of a front-looking holographic radar along the x-axis as a function of the angle φ 61

Figure 3.7 The resolution of a front-looking holographic radar along the z-axis as a function of the angle φ 62
Figure 3.8 Generalised schemes of hologram recording (a) and reconstruction (b) 63
Figure 3.9 Recording (a) and reconstruction (b) of a two-point object for finding longitudinal magnifications: 1, 2 – point objects, 3 – reference wave source and 4 – reconstructing wave source 67
Figure 3.10 The focal depth of a microwave image: 1 – reconstructing wave source, 2 – real image of a point object and 3 – microwave hologram 68
Figure 3.11 The basic geometrical relations for a spot-light SAR 70

Chapter 4

Figure 4.1 The geometrical relations in a SAR 85
Figure 4.2 A generalised block diagram of a SAR 85
Figure 4.3 The variation of the parameter Q with the synthesis range L_s at $\lambda = 3$ cm, $\Theta = 0.02$ and various values of R 90
Figure 4.4 The dependence of the spatial correlation range of the image on normalised L_s for multi-ray processing (solid lines) at various degrees of incoherent integration D_e and for averaging of the resolution elements (dashed lines) at various G_e : $\lambda = 3$ cm, $R = 10$ km; 1, 5–0 (curves overlap); 2, 6–$0.25(\lambda R/2)^{1/2}$; 3, 7–$(\lambda R/2)^{1/2}$; 4, 8–$2.25(\lambda R/2)^{1/2}$ 91
Figure 4.5 The variation of the parameter Q_h with the number of integrated signals N_i at various values of K_a 93
Figure 4.6 The variation of the parameter Q_e with the synthesis range L_s at various signal correlation times τ_c 97
Figure 4.7 The parameter Q as a function of the synthesis range L_s at various signal correlation times τ_c 98

Chapter 5

Figure 5.1 A schematic diagram of direct bistatic radar synthesis of a microwave hologram along arc L of a circle of radius R_0: 1 – transmitter, 2 – receiver 102
Figure 5.2 A schematic diagram of inverse synthesis of a microwave hologram by a unistatic radar located at point C 103
Figure 5.3 The geometry of data acquisition for the synthesis of a 1D microwave Fourier hologram of a rotating object 103
Figure 5.4 Optical reconstruction of 1D microwave images from a quadrature Fourier hologram: (a) flat transparency, (b) spherical transparency 106
Figure 5.5 The dependence of microwave image resolution on the normalised aperture angle of the hologram 109

Figure 5.6 Microwave images reconstructed from Fourier holograms: (a) quadrature hologram, (b) complex hologram with carrier frequency, (c) complex hologram without carrier frequency and (d,e,f) the variation of the reconstructed image with the hologram angle ψ_s (complex hologram without carrier frequency) 113

Figure 5.7 The algorithm of digital processing of 1D microwave complex Fourier holograms 114

Figure 5.8 A microwave image of a point object, reconstructed digitally from a complex Fourier hologram as a function of the object's aspects $\Psi_0(\Psi_s = \pi/6)$: (a) $\Psi_0 = \pi/12$, (b) $\Psi_0 = 5\pi/2$ and (c) $\Psi_0 = 3\pi/4$. 115

Chapter 6

Figure 6.1 The aspect variation relative to the line of sight of a ground radar as a function of the viewing time for a satellite at the culmination altitudes of 31°, 66° and 88°: (a) aspect α and (b) aspect β 121

Figure 6.2 Geometrical relations for 3D microwave hologram recording: (a) data acquisition geometry; *a–b*, trajectory projection onto a unit surface relative to the radar motion and (b) hologram recording geometry 123

Figure 6.3 The sequence of operations in radar data processing during imaging 125

Figure 6.4 Subdivision of a 3D microwave hologram into partial holograms: (a) 1D partial (radial and transversal), (b) 2D partial (radial and transversal) and (c) 3D partial holograms 128

Figure 6.5 Subdivision of a 3D surface hologram into partial holograms: (a) radial, (b) 1D partial transversal and (c) 2D partial 129

Figure 6.6 Coherent summation of partial hologram. A 2D narrowband microwave hologram: (a) highlighting of partial holograms and (b) formation of an integral image 132

Figure 6.7 Coherent summation of partial hologram. A 2D wideband microwave hologram: (a) highlighting of partial holograms, (b) formation of an integral image 133

Figure 6.8 The computational complexity of the coherent summation algorithms as a function of the target dimension for a narrowband microwave hologram: (a) transverse partial images, (b) hologram samples 137

Figure 6.9 The relative computational complexity of coherent summation algorithms as a function of the target dimension for a narrowband microwave hologram: (a) transverse partial images/CCA, (b) hologram samples/CCA 140

Figure 6.10 The relative computational complexity of coherent summation algorithms of hologram samples and transverse partial images versus the coefficient μ in the case of a wideband hologram 141
Figure 6.11 The relative computational complexity of coherent summation algorithms for radial and transverse partial images versus the coefficient μ in the case of a wideband hologram 142
Figure 6.12 The transformation of the partial coordinate frame in the processing of a 3D hologram by coherent summation of transverse partial images 143

Chapter 7

Figure 7.1 Characteristics of an imaging device in the case of partially coherent echo signals: (a) potential resolving power at $C_2 = 1$, (b) performance criterion ($1 - d_c = 6.98$ m, $2 - d_c = 3.49$ m and $3 - d_c = 0$) 151
Figure 7.2 Typical errors in the impulse response of an imaging device along the s-axis: (a) response shift, (b) response broadening, (c) increased amplitude of the response side lobes and (d) combined effect of the above factors 153
Figure 7.3 The resolving power of an imaging device in the presence of range instabilities versus the synthesis time T_s and the method of resolution step measurement: (a) $-\sigma_p = 0.04$ m; 1 and 1′ (2 and 2′) – first (second) way of resolution step measurement; 1 and 2 – $T_c = 1.5$ s, 1′ and 2′ – $T_c = 3$ s; (b) $-\sigma_p = 0.05$ m, 1 and 1′ (2 and 2′) – first (second) way of resolution step measurement; 1 and 2 – $T_c = 1.5$ s, 1′ and 2′ – $T_c = 3$ s 154
Figure 7.4 The resolving power of an imaging system in the presence of velocity instabilities versus the synthesis time T_s and the method of resolution step measurement: (a) $\sigma_{x'y'} = 0.1$ m/s (other details as in Fig. 7.3), (b) $\sigma_{x'y'} = 0.2$ m/s (other details as in Fig. 7.3) 155
Figure 7.5 Evaluation of the performance of a processing device in the case of partially coherent signals versus the synthesis time T_s and the space step of path instability correlation d_c: 1–$d_c =$ 6.98m, $2 - d_c = 3.49$ m 155

Chapter 8

Figure 8.1 The normalised refractive index spectrum $\Phi_n(\chi)/C_n^2$ as a function of the wave number χ in various models: 1 – Tatarsky's model-I, 2 – Tatarsky's model-II, 3 – Carman's model and 4 – modified Carman's model 160
Figure 8.2 The profile of the structure constant C_n^2 versus the altitude for April at the SAR wavelength of 3.12 cm 164
Figure 8.3 The profile of the structure constant C_n^2 versus the altitude for November at the SAR wavelength of 3.12 cm 165

Figure 8.4 A geometrical construction for a spaceborne SAR tracking a point object A through a turbulent atmospheric stratum of thickness h_t 168
Figure 8.5 A schematic test ground with corner reflectors for investigation of SAR performance 176
Figure 8.6 A 1D SAR image of two corner reflectors 177
Figure 8.7 A histogram of the noise distribution in a SAR receiver 178
Figure 8.8 The grey-level (half-tone) resolution versus the number of incoherently integrated frames N 179
Figure 8.9 The dependence of the image interpretability on the resolution versus linear resolution $p_a = p_r = p$ 180
Figure 8.10 The dependence of the half-tone resolution on the number of incoherent integrations over the total real antenna pattern 181

Chapter 9

Figure 9.1 The mean monthly convoy speed in the NSR changes from V_0 (without satellite data) to V_1 (SAR images used by the icebreaker's crew to select the route in sea ice). The mean ice thickness (h_i) is shown as a function of the season. (N. Babich, personal communications) 198
Figure 9.2 (a) Photo of grease ice and (b) a characteristic dark SAR signature of grease ice. ©European Space Agency 199
Figure 9.3 Photo of typical nilas with finger-rafting 200
Figure 9.4 A RADARSAT ScanSAR Wide image of 25 April 1998, covering an area of 500 km × 500 km around the northern Novaya Zemlya. A geographical grid and the coastline are superimposed on the image. ©Canadian Space Agency 201
Figure 9.5 A RADARSAT ScanSAR Wide image of 3 March 1998, covering the boundary between old and first-year sea ice in the area to north Alaska. ©Canadian Space Agency 202
Figure 9.6 (a) Photo of a typical pancake ice edge and (b) a characteristic ERS SAR signature of pancake ice. A mixed bright and dark backscatter signature is typical for pancake and grease ice found at the ice edge. ©European Space Agency 203
Figure 9.7 A RADARSAT ScanSAR Wide image of 8 May 1998, covering the south-western Kara Sea. ©Canadian Space Agency 204
Figure 9.8 An ENVISAT ASAR image of 28 March 2003, covering the ice edge in the Barents Sea westward and southward of Svalbard. ©European Space Agency 205
Figure 9.9 An ERS-2 SAR image of 11 September 2001, covering the Red Army Strait in the Severnaya Zemlya Archipelago. ©European Space Agency 206

Figure 9.10 An ERS-2 SAR image (100 km × 100 km) taken on 24 June 2000 over the Black Sea (region to the East Crimea peninsula) and showing upwelling, natural films 208
Figure 9.11 SST retrieved from a NOAA AVHRR image on 24 June 2000. 209
Figure 9.12 A fragment of an ERS-2 SAR image (26 km × 22 km) taken on 30 September 1995 over the Northern Sea near the Norwegian coast and showing swell 210
Figure 9.13 An ERS-2 SAR image (100 km × 100 km) taken on 28 September 1995 over the Northern Sea and showing an oil spill, wind shadow, low wind and ocean fronts 211
Figure 9.14 An ERS-1 SAR image (100 km × 100 km) taken on 29 September 1995 over the Northern Sea showing rain cells 213
Figure 9.15 An ERS-2 SAR image (18 km × 32 km) taken on 30 September 1995 over the Northern Sea showing an internal wave and a ship wake 214
Figure 9.16 The scheme of the reconstruction algorithm 221
Figure 9.17 A typical 1D image of a perfectly conducting cylinder 222
Figure 9.18 The local scattering characteristics for a metallic cylinder (E-polarisation) 223
Figure 9.19 The local scattering characteristics for a metallic cylinder (H-polarisation) 224
Figure 9.20 A mathematical model of a radar recognition device 226

Introduction

The analysis of the current state and tendencies in radar development shows that novel methods of target viewing are based on a detailed study of echo signals and their informative characteristics. These methods are aimed at obtaining complete data on a target, with emphasis on revealing new steady parameters for their recognition. One way of raising the efficiency of radar technology is to improve available methods of radio vision, or imaging. Radio vision systems provide a high resolution, considerably extending the scope of target detection and recognition. This field of radar science and technology is very promising, because it paves the way from the classical detection of a point target to the imaging of a whole object.

The physical mechanism underlying target viewing can be understood on a heuristic basis. An electromagnetic wave incident on a target induces an electric current on it, generating a scattered electromagnetic wave. In order to find the scattering properties of the target, we must visualise its elements making the greatest contribution to the wave scattering. This brings us to the concept of a radar image, which can be defined as a spatial distribution pattern of the target reflectivity. Therefore, an image must give a spatial quantitative description of this physical property of the target with a quality not less than that provided by conventional observational techniques.

Radio vision makes it possible to sense an object as a visual picture. This is very important because we get about 90 per cent of all information about the world through vision. Of course, a radar image differs from a common optical image. For instance, a surface rough to light waves will be specular to radio waves (microwaves), and images of many objects will look like bright spots, or glare. However, the representation of information transported by microwaves as visual images has become quite common. It took much time and effort to get a high angular resolution in the microwave frequency band because of the limited size of a real antenna. It was not until the 1950–1960s that a sufficiently high resolution was obtained by a side-looking radar with a large synthesised antenna aperture. The synthetic aperture method was then described in terms of the range-Doppler approach.

At about the same time, a new method of imaging in the visible spectrum emerged which was based on recording and reconstruction of the wave front and its phase, using a reference wave. A lens-free registration of the wave front (the holographic technique), followed by the image reconstruction, was first suggested by D. Gabor in